Title
A prototype silicon double quantum dot with dispersive microwave readout

Journal
Journal of Applied Physics, 116(4)

ISSN
0021-8979

Authors
Schmidt, AR
Henry, E
Lo, CC
et al.

Publication Date
2014-07-28

DOI
10.1063/1.4890835

Peer reviewed

A prototype silicon double quantum dot with dispersive microwave readout

A. R. Schmidt,[1,*] E. Henry,[1] O. Namaan,[1,†] C. C. Lo,[2,‡] Y. -T. Wang,[2] H. Li,[3,4] L. Greenman,[4] T. Schenkel,[5] K. B. Whaley,[4] J. Bokor,[2] E. Yablonovitch,[2] and I. Siddiqi[1,§]

[1] *Quantum Nanoelectronics Laboratory, Department of Physics, University of California, Berkeley, California 94720, USA*
[2] *Department of Electrical Engineering and Computer Sciences, University of California, Berkeley, California 94720, USA*
[3] *Department of Physics, University of California, Berkeley, California 94720, USA*
[4] *Department of Chemistry, University of California, Berkeley, California 94720, USA*
[5] *Accelerator and Fusion Research Division, Lawrence Berkeley National Laboratory, Berkeley, California 94720, USA*

(Dated: February 19, 2014)

We present a unique design and fabrication process for a lateral, gate-confined double quantum dot in an accumulation mode metal-oxide-semiconductor (MOS) structure coupled to an integrated microwave resonator. All electrostatic gates for the double quantum dot are contained in a single metal layer, and use of the MOS structure allows for control of the location of the two-dimensional electron gas (2DEG) via the location of the accumulation gates. Numerical simulations of the electrostatic confinement potential are performed along with an estimate of the coupling of the double quantum dot to the microwave resonator. Prototype devices are fabricated and characterized by transport measurements of electron confinement and reflectometry measurements of the microwave resonator.

PACS numbers: 85.35.Be, 73.63.Kv, 81.07.Ta, 73.21.La, 03.67.Lx, 84.40.Dc

I. INTRODUCTION

The ability to trap individual electrons in semiconductor quantum dots has lead to great progress towards enabling full quantum manipulation of their charge and spin in nanoscale solid state devices[1–3]. In particular there has been much interest in realizing charge[4–6] and spin qubits[2, 3, 7, 8] in lateral double quantum dots due to the ability to tune the qubit energy splitting via an electrostatic gate to control the tunnel coupling between the individual quantum dots[1, 4]. Readout of quantum dots has traditionally been performed by direct current transport measurements, either through the double quantum dots[1], or by using an auxiliary current-biased quantum point contact (QPC) to monitor the charge state[2, 3]. More recently, embedding the QPC in a LC tank circuit with a resonant frequency of ∼100-400 MHz has enabled faster, single-shot readout by non-dispersively monitoring the loss on resonance[3, 9].

Circuit quantum electrodynamics (cQED) in superconducting qubits has enabled fast, quantum non-demolition measurements. This is accomplished by coupling the superconducting qubits to a several gigahertz frequency microwave resonator via the qubit transition electric dipole moment, a quantum interaction that is well described by the Jaynes-Cumming Hamiltonian[10]. When the qubit and resonator are detuned by many linewidths, the interaction is dispersive and readout via the resonator microwave field is a fully quantum non- demolition measurement[12]. This has allowed coupling multiple qubits via the resonator[13], continuous weak measurement[14], creation of flying qubits[15], initial state purification[16], and stabilization of the qubit Rabi state via quantum feedback[17].

In this paper we report a unique design for a microwave resonator coupled double quantum dot in Si, with the goal of integrating the cQED architecture with semiconducting qubits. The coupling is very similar to that reported in previous resonator-coupled GaAs/AlGaAs double quantum dots[18, 19], with the resonator conductors connected to the double dot plunger gates so that the microwave voltage directly couples to the Fermi levels, and hence the charge states, of the dots. Our quantum dot is an electrostatically gate defined, silicon metal-oxide-semiconductor (MOS) structure utilizing accumulation mode field effect to create a two-dimensional electron gas (2DEG). This allows for lithographically fabricated accumulation gates to determine where the 2DEG will exist in the substrate and keep it spatially decoupled from the microwave resonator, limiting high frequency loading from the 2DEG conductivity and capacitance. In contrast, the chemically defined 2DEG in GaAs/AlGaAs heterostructures must be etched away before fabricating the resonator. Using Si also eliminates piezoelectric acoustic phonon coupling[20] which has been implicated in loss and limiting coherence times in GaAs/AlGaAs devices[4, 19]. Finally, Si has the potential for long spin coherence due to small spin-orbit coupling[3, 20] and the possibility to eliminate the nuclear spin bath by isotopic purification[21]; singlet-triplet spin qubits in Si/SiGe[8] without purification have T_2^* an order of mag-

* andrewrobertschmidt@gmail.com
† Present address: Northrup-Grumman
‡ Present address: London Centre for Nanotechnology, University College London, London WC1H 0AH, UK
§ irfan_siddiqi@berkeley.edu

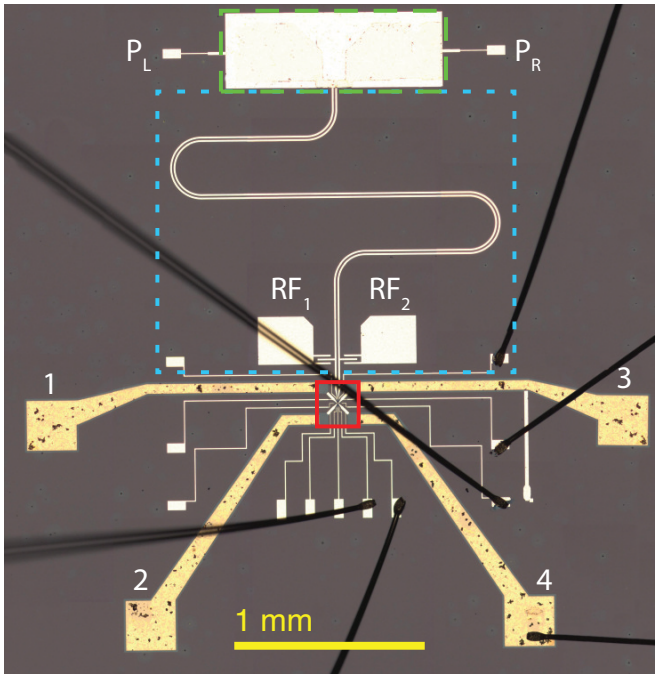

FIG. 1. (color online) Large scale view of the device. The electron confinement gates are located within the red solid box and are not visible on this scale. The 'X' within this box are the two accumulation gates creating the 2DEG. Inside the short dashed blue box lies the CPS resonator and the coupling capacitors for the microwave wire bond feed. Within the long dashed green box lies the ∼50pF shorting capacitor that is the bias tee combining the DC P_L and P_R bias voltage with the microwave carrier.

nitude longer than in the typical GaAs[7] devices.

While the double-dot/resonator coupling is via the qubit electric dipole moment, the ultimate goal is to couple the semiconductor spin degree of freedom, which in Si has a lifetime approaching ∼1s[3, 21–23]. At an estimated coupling rate of tens of hertz, directly coupling the electron spin magnetic field to the resonator is nearly impossible for cQED. Instead, our design would employ electric dipole spin resonance (EDSR)[24–26] via a strong magnetic field gradient[26] to couple the spin to the resonator. The precise technique to add the field gradient we leave for future work, and is itself not a trivial fabrication process. The first steps towards using EDSR to couple the spin to a microwave resonator have recently been demonstrated by using the microwave resonator to readout the spin state of a double quantum dot in InAs nanowires via strong spin-orbit EDSR[27].

The layout of this paper is as follows. In Section II we describe the device geometry and fabrication details. In Section III we discuss the numerical simulations that were used to guide device design. Section IV contains the results of experimental characterization of device functionality and Section V contains a brief summary and conclusions.

II. DEVICE LAYOUT AND FABRICATION PROCESS

Fig. 1 is an optical image of our resonator coupled double quantum dot at the largest length scales of the device. The short dashed blue box outlines the microwave resonator, which is a shorted, 6 GHz quarter-wavelength section of coupled microstrip. The long dashed green box outlines the shorting termination. This is actually a ∼50 pF capacitor which is a short at 6 GHz, but is an open at low frequencies allowing us to individually DC bias each resonator conductor. At the antinode, the resonator conductors connect to the left and right plunger gates of each quantum dot, which are within the solid red box. The 'X' shaped structure within this box are the two metal-oxide accumulation gates beneath which the 2DEG is located at the semiconductor-oxide interface. These gates are labeled T_R and T_L in Fig. 2(a). This is a standard MOS geometry with mobile electrons for the 2DEG coming from the n-type degenerately doped ohmic contacts. A positive bias on these gates accumulates the 2DEG. The ohmics contacts are labeled 1-4 in Fig. 1. RF_1 and RF_2 are the wire bond pads for the microwave carrier, which is coupled to the resonator via finger capacitors and differentially excited with a 180° hybrid. These bond pads are large to minimize inductance. Also visible in the figure are several Si doped Al wire bonds. They are attached to a much smaller set of bond pads for the DC biases, and their small size is chosen to reduce the electron-beam write time in the lithography step. We have not found these to be difficult to wire bond. The thin size of the leads from these pads to the rest of the device is to increase the series inductance and choke out any residual high frequency noise.

Fig. 2(a) shows a SEM image of the accumulation metal-oxide gates, false-colored in red and labeled T_R and T_L, that determine the location of the 2DEG in the vicinity of the quantum dot electron confinement gates. The resonator conductors are false colored-blue and are also the plunger gates for the two dots, P_L and P_R. The resonator conductors are well decoupled from the 2DEG as shown by the spatial separation in this figure. The inset focuses on these confinement gates, with a length scale very similar to that successfully used in previous Si quantum dots[5, 28, 29].

The confinement gates are a mostly standard set of quantum dot confinement gates; however, the plunger gates controlling the dot charge states are unique in that they are operated in accumulation mode at positive bias. Their vertical orientation should reduce the capacitive division of the applied bias, as observed in other Si MOS double quantum dots with accumulation mode plunger gates[30]. This should help maximize the coupling of the ground state quantum voltage fluctuations of the resonator differential mode into the double dot. The depletion mode side gates are labeled $L_{T,B}$ and $R_{T,B}$, and the U gate controls the tunnel coupling between the left and right dots. The QPC gates are $Q_{L,R}$

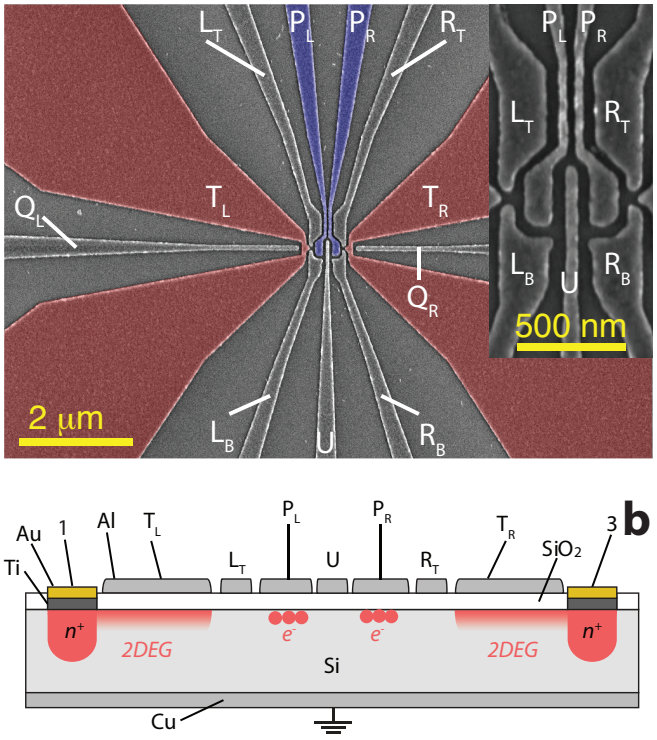

FIG. 2. (color online) **(a)** SEM of the electron confinement gates and the 2DEG accumulation gates, which are false colored red. The plunger gates P_R and P_L are false colored blue, and emphasize the spatial decoupling of the microwave resonator from the 2DEG. The inset SEM details the electron confinement gates. **(b)** A schematic cross section of the MOS accumulation structure in this device. (not to scale)

The devices are fabricated from commercially available Si wafers from Topsil that are float-zone grown in the $\langle 100 \rangle$ orientation, n-type with room temperature resistivity in excess of 10 kΩ-cm, and so are very clean. Special care must taken with devices made from these wafers due to the increased susceptibility to ESD damage in the metal-oxide gates. Fabrication begins with ion-implantation of the phosphorous donors in the ohmic contact regions. These must be degenerately doped beyond the metal-insulator transition to ensure device operation below liquid He temperatures. This is followed by creation of the 100nm thick native SiO_2 gate oxide barrier by thermal oxidation at 1000°C. Next, this oxide on the ohmic contacts is etched away with HF and metal contacts are deposited consisting of 5nm Ti on the bare Si surface and 40nm Au on top for the wirebond pads. After this is the e-beam write for the metal lithography, defining the gates, resonator conductors, metal leads and wire bond pads. With the exception of the ohmic contacts, all other metal is 20nm thick Al deposited in a custom built e-beam evaporator designed for fabrication of superconducting qubits[16, 17]. Finally the shorting capacitor is finished. The dielectric is 200nm thick CVD SiO_2 and above this is the 50nm Al upper capacitor plate. A schematic cross section of the device, showing the metal-oxide structures but excluding the shorting capacitor is shown in Fig. 2(b), emphasizing that all the confinement and accumulation gates are defined in a single metal layer. The final step is a forming gas anneal to clean the oxide interfaces.

Similar MOS devices built using these fabrication techniques are measured to have a mobility of 10,000 -15,000 cm^2/V s at 4.2K[31]. This is comparable to previous Si MOS quantum dots[3, 22].

III. NUMERICAL SIMULATIONS

To simulate the device we first find the electrostatic confinement potential by numerically and self consistently solving Poission's equation with the accumulated 2DEG charge density given in the semiclassical Thomas-Fermi approximation[32, 33]:

$$\begin{aligned} \nabla \cdot (\kappa \nabla \phi(\mathbf{r})) &= -4\pi \rho_{2DEG}(\mathbf{r}) \\ \rho_{2DEG}(\mathbf{r}) &= -e \frac{m_t^*}{\pi \hbar^2}(E_F - E_0)\delta(z) \qquad E_F > E_0 \\ \rho_{2DEG}(\mathbf{r}) &= 0 \qquad\qquad\qquad\qquad\quad E_F < E_0 \end{aligned}$$

Here κ is the material-dependent dielectric constant, $\phi(\mathbf{r})$ is the electrostatic potential, ρ_{2DEG} is the 2DEG charge density, m_t^* is the Si transverse electron effective mass, E_F is the Fermi energy, and E_0 is the energy of the bottom of the lowest 2DEG subband. The Si-SiO_2 interface is at $z = 0$ and perpendicular to the z direction, and by using $\delta(z)$ we are ignoring the spatial extent of the wave function in the direction of confinement. Since field-effect 2DEGs in Si-SiO_2 are typically within ∼5nm of the interface and are of the same order in extent[32], this is a very good approximation. The valley degeneracy is ignored. Space charges are ignored, due to the high room temperature resistivity of the wafers. Oxide and interface charges are ignored. E_0 implicitly depends on $\phi(\mathbf{r})$, essentially because the gate bias must bend the conduction band below E_F before the 2DEG can form. The result is that a threshold bias V_T[32, 34] must be applied before the 2DEG forms; we measured this to be 1.2-1.4V before transport occurs in our devices. The commercial program COMSOL Multiphysics was used[35] for the numerical solution. The resulting 2DEG density is shown in Fig. 3(a) for the applied gate bias boundary conditions shown in Fig 3(c). This 2DEG density is comparable to that used in GaAs devices.

The resulting electrostatic potential at the Si-SiO_2 interface is shown in Fig. 3(b). The thin white lines in this figure are equipotential lines with 5 mV spacing, and we find electrostatic potential maxima below the two plunger gates $P_{L,R}$. Multiplying by the electron charge $-e$, these become potential energy minima of ∼20 meV for confining electrons in the quantum dots. The double quantum dot ground and first excited state energies and wave

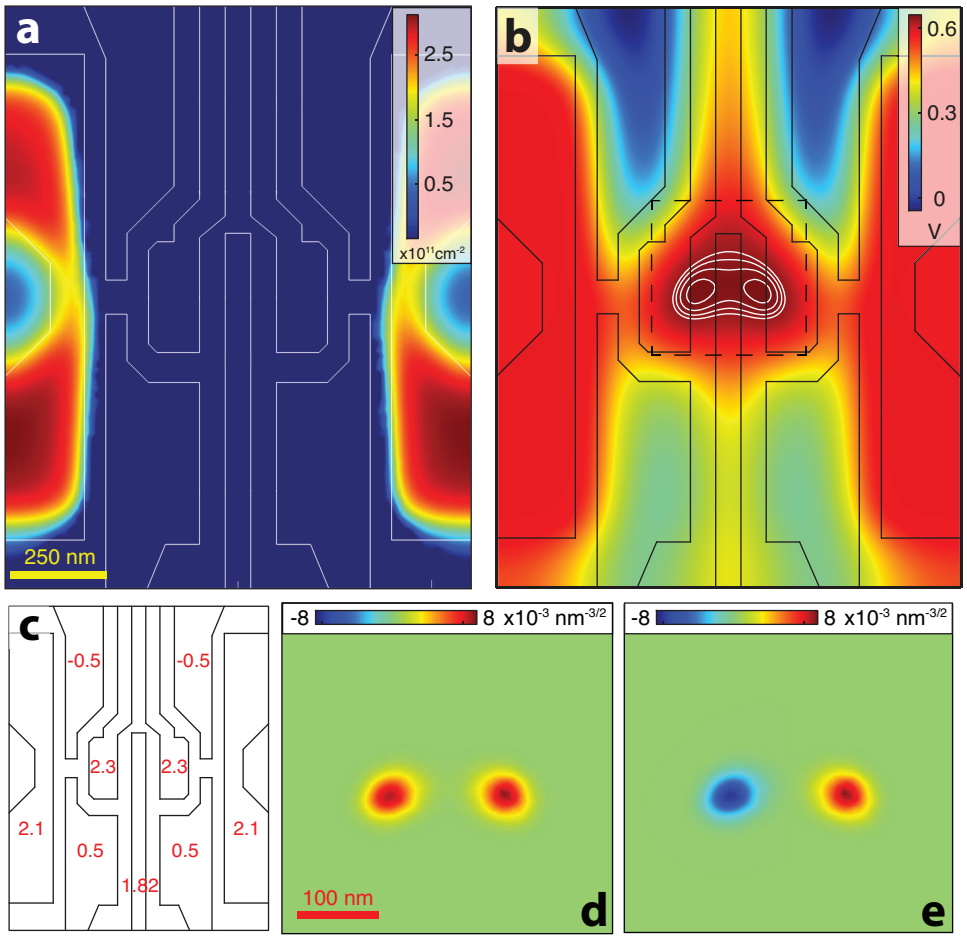

FIG. 3. (color online) Numerical simulations (see text for details) **(a)** 2DEG induced at the Si-SiO_2 interface **(b)** Interface electrostatic potential. **(c)** Applied gate bias voltages setting boundary conditions. **(d)** Ground state wave function envelope for the region in the black dashed box in (b). **(e)** First excited state wave function envelope.

function envelopes are found within the effective mass approximation[32, 33] by using COMSOL to numerically solve Schrödinger's equation with this electrostatic potential energy, again using the anisotropic effective mass of silicon. The ground state wave function envelope is shown in Fig. 3(d) for the region within the black dashed line in Fig. 3(b), and shows the bonding symmetry. The first excited state envelope for the same region is shown in Fig. 3(e) with the anti-bonding symmetry, and has a 3 GHz ground state energy difference.

Coupling a double quantum dot charge qubit[36] to a microwave resonator is identical to coupling a Cooper pair box superconducting qubit[11] to the same resonator. At the charge degeneracy point, the Jaynes-Cummings Hamiltonian with qubit frequency ω_q, resonator frequency ω_r, and qubit-resonator coupling g_0 is

$$H_{\rm JC} = \frac{1}{2}\hbar\omega_{\rm q} + \frac{1}{2}\hbar\omega_{\rm r}a^\dagger a + \hbar g_0(a^\dagger\sigma_- + a\sigma_+)$$
$$g_0 = \frac{eV^0_{\rm rms}}{\hbar}\alpha$$

Here, $a^\dagger$ creates a resonator photon, and $\sigma_{+/-}$ are the qubit Pauli operators. In the coupling term, $V^0_{\rm rms}$ is the resonator ground state R. M. S. voltage fluctuation, and $\alpha = C_{\rm g}/C_\Sigma$ is the lever arm describing the voltage division of the plunger capacitance $C_{\rm g}$ by the total capacitance to ground C_Σ. This coupling term g_0 is the same for both charge double quantum dots and Cooper pair box qubits at charge degeneracy. Because both have similar α and similar $V^0_{\rm rms}$ owing to similar planar transmission line structures, the coupling rate $g_0/\hbar$ is observed to be the same order of magnitude at 10-50 MHz[10, 18, 19, 27] for both types. We expect our Si device operated as a charge qubit to be similar.

IV. EXPERIMENTAL CHARACTERIZATION

All experiments were performed in an Oxford Instruments Triton cryogen-free dilution refrigerator at temperatures below 15 mK. All low frequency measurement wiring is filtered at the mixing chamber, first through a lossy Eccosorb CR124 100 MHz low pass filter, which

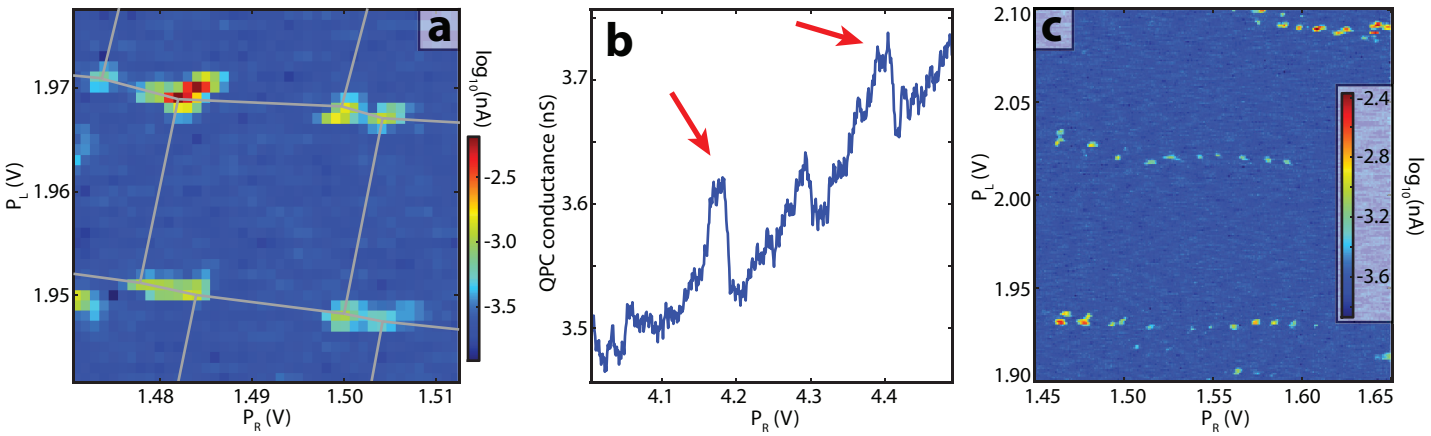

FIG. 4. (color online) Transport characterization of electron confinement. **(a)** Current resonances as function of plunger gate bias forming honeycomb charge stability regions. **(b)** QPC conductance as a function of left plunger gate bias showing single electron charing events (arrows). **(c)** Inconsistent honeycombs over large plunger gate bias ranges.

has been demonstrated to attenuate frequencies up to 40GHz[37]. This is followed by a surface mount RC π low pass filter with a 1kHz cutoff.

To test the ability to confine charge, we made a series of DC electronic transport measurements in a device similar to the one in Figs 1-2(a). Figure 4(a) shows a plot of current through the device on a log scale as a function of bias voltage on the left and right plunger gates $P_{L,R}$. Ohmic contacts 1 and 4 form the source and drain with bias voltage of 100 μV in a standard AC lock-in technique at 13Hz using a Stanford Research Systems SR810. Overlain on top of this is the a honeycomb charge stability diagram expected for transport through a double quantum dot in Coulomb blockade[1, 3] and analysis of this yields plunger gate capacitances of 0.3-0.4 aF.

The left QPC is biased by applying a 1 nA current bias to ohmics 1-2, while a bias voltage on Q_L brings this channel close to pinch-off. The QPC conductance measured with the same lock-in technique above is shown in Figure 4(a) as a function of left plunger P_L voltage. Red arrows mark peaks due to charging events in the left dot, which are repeatable. Figures 4(a)-(b) indicate that our double quantum dot is indeed exhibiting single electron charging.

However, when we try and to measure charge stability from transport through the dots over a wider range of gate bias, we find the current resonances shown in Fig 4(c). We cannot get consistent honeycomb patterns over a large bias range. A qualitative explanation for this is given in the Summary, Sec. V.

In Fig 4(a), gates $T_{R,L}$, $Q_{R,L}$ were biased at 4 V, while $L_{T,B}$, $R_{T,B}$, and U were 1 V. In Fig 4(c), $T_{R,L}$, $Q_{R,L}$ were at 4 V, $L_{T,B}$, $R_{T,B}$ at 1.2V, and U was at 0.95 V. For Fig 4(d), these gates were in a different bias regime. T_L was 4.5 V, and Q_L was 401.5mV below T_L to put the QPC near pinch-off. The side gates $L_{T,B}$, $R_{T,B}$ were at -1.5V to shut off transport from the quantum dot to the 2DEG, and U was also at -1.5V to isolate the two dots. The negative biases on these confinement gates required the larger compensating plunger gate voltages in Fig 4(b).

Microwave measurements of the resonator were made in reflection using a vector network analyzer (VNA). The incoming microwaves are thermalized with 20 dB at 4K, 20dB at the still, and 20 dB at base temperature on the mixing chamber. From there they are sent though a circulator to reflect off the device and on return pass

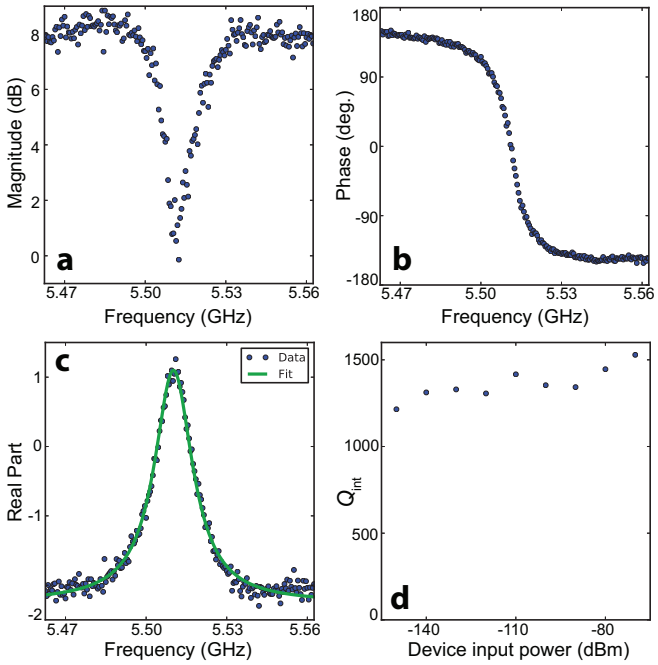

FIG. 5. (color online) Microwave resonator reflection coefficient data **(a)** Magnitude, including overall gain of the measurement chain. **(b)** Phase **(c)** Real part, with time delay adjusted to adjust reference to input plane of resonator. The fit is to a Lorentzian. **(d)** Power dependence of the internal quality factor, characterizing resonator internal losses.

through an additional isolator to a NbTi superconducting coaxial line connecting to the LNF HEMT amplifier at 4K.

Fig. 5(a) shows measurements of the reflected amplitude at -150 dBm input power, including the overall system gain, and Fig. 5(b) shows the phase. The wirebond pads were connected to a 180° hybrid for differential excitation via 1 cm wire bonds connected to $RF_{1,2}$ in Fig. 1. This adds series inductance, modifying the complex impedance away from the Lorentzian approximation for a resonator. Assuming the wire bond impedance is purely reactive, we fit the real part of the reflection, removing the time delay so that the reflection data is measured with respect to resonator. The resulting fit to a Lorentzian is very good, as shown in Fig. 5(c) for -150 dBm. From the fit we extract a resonant frequency f_0 of 5.511 GHz, which is down from the 6 GHz set by the transmission line length due to the reactive loading of the wire bonds and coupling capacitors. The resonator Q of 307 breaks down to an external $Q_{\rm ext}$ of 411 and an internal $Q_{\rm int}$ of 1210, so that the resonator is over-coupled. This Q translates to a half-power bandwidth of 18 MHz, which would allow measurement of fast charge dynamics.

The power dependence of $Q_{\rm int}$ is plotted in Fig. 5(d) from -150 dBm to -70 dBm. Using $\bar{n} = 4P_{\rm in}Q^2/(Q_{\rm ext}\hbar\omega_0)$, where $P_{\rm in}$ is the steady state input power, this corresponds to an average photon number $\bar{n}$ of order 0.01 to 10^6. Over this range $Q_{\rm int}$ is observed to climb from 1210 to 1530. To demonstrate that this loss is due to the CVD SiO_2 dielectric in the shorting capacitor, we have fabricated a device with this capacitor replaced by an Al shorting stub and measure $Q_{\rm int}$ to be above 10,000 at -150 dBm for a $Q_{\rm ext}$ of 2000. This CVD SiO_2 internal loss and internal loss power dependence is far less than previously reported for LC resonator capacitors[38] or for coplanar waveguide (CPW) transmission line resonators[39]. This may be due to the fact that for our devices the shorting capacitor is at a voltage node where the resonator voltage is minimal, but more comprehensive work is required to demonstrate this.

V. SUMMARY

We have designed and developed a fabrication process for a Si double quantum dot coupled to a microwave resonator. We have performed simple numerical simulations to verify dot charge confinement, and estimate the double dot - resonator vacuum coupling strength. We have fabricated test devices and characterized the quantum dot charge confinement through DC transport measurements and the microwave resonator spectrum with a VNA. The resonant frequency is 5.511GHz with $Q_{\rm int}/Q_{\rm ext} = 3$ in the overcoupled regime, while the total $Q = 307$ gives a line width of 18 MHz. The over-coupling allows for pulsed time-domain detection of dispersive resonant frequency shifts in the phase of a homodyne measurement. The fastest resolvable phase change is ∼60 ns, set by the inverse line width, which is well within the charge relaxation T_1 seen in Si charge qubits[6].

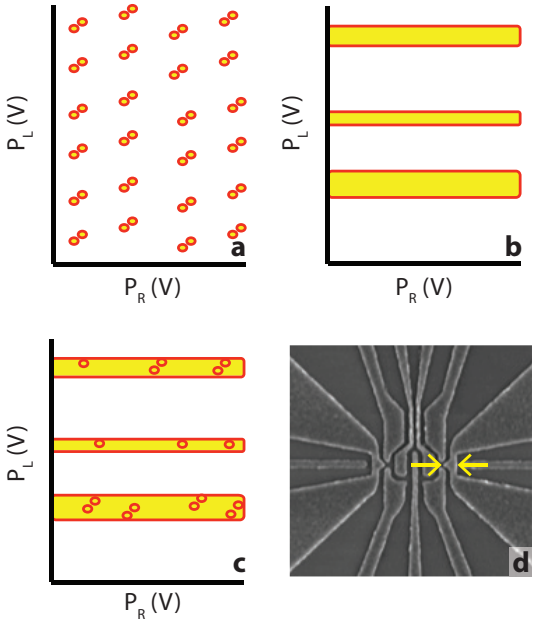

FIG. 6. (color online) Schematic representation for the failure to achieve consistent long range honey combs with sweeps of plunger gate bias. **(a)** Cartoon of the double quantum dot honeycomb current peaks as a function of gate bias. **(b)** Cartoon of the sub two- dimensional conductance in the region marked by arrows in (d), giving regions of allowed conductance, marked in yellow, surrounded by regions of forbidden conductance. **(c)** Cartoon of what transport measurements of (a) and (b) in series would look like. **(d)** The region of the accumulation gate marked with the yellow arrows is where the 2DEG becomes sub two-dimensional.

The DC transport measurements demonstrate charge confinement for the device, but Fig. 4(c) shows that the charge stability honeycombs are not found over a wide enough gate bias range. One explanation for this is that the 2DEG accumulation gates $T_{L,R}$ become too narrow where they come near the confinement gates $L_{T,B}$ and $R_{T,B}$, as shown between the arrows in Fig 6(d), so that the 2DEG in fact becomes sub two-dimensional in this region. Then our double quantum dot, with honeycomb current resonances shown schematically in Fig. 6(a) is in series with short, sub 2D channels with regions of allowed and forbidden conductance, shown schematically in Fig. 6(c), and the resulting total series conductance is shown schematically in Fig. 6(c). This is a very qualitative representation of the data in Fig. 4(c).

In hindsight, this problem can be identified in the 2DEG density simulation shown in Fig. 3(a) by noting that the 2DEG density drops and becomes non-uniform over very short lengths where $T_{L,R}$ narrow at the gap between the confinement gates $L_{T,B}$ and $R_{T,B}$. However, due to the use of the semi-classical Thomas Fermi approximation the lowering of dimensionality is not properly captured. The solution to this is to make the narrow

part of the gates, shown between the Fig. 6(d) arrows, wider to ∼300nm, or ∼30 times the Si transverse effective mass Thomas-Fermi screening length[32, 33].

After this, there is more non-trivial testing to be done. One test is to demonstrate that the double dot can be completely depleted of electrons, so that the few-electron regime can be reached, followed by showing that the splitting of the lowest two valleys is large, similar to the 100-750μV measured in previous Si MOS quantum dots[3]. Both of these are necessary for spin manipulation of Si double dot devices. Simultaneously with this is demonstration of dispersive readout of the honeycomb charge stability diagrams with the microwave resonator, as done previously in III-V devices[18, 19, 27]. Attempts will be made to make a simple charge qubit and use the resonator for dispersive readout in pulsed time-domain experiments.

ACKNOWLEDGMENTS

The authors thank K. C. Nowack, O. E. Dial, O. Namaan, K. Murch, and R. Vijay for helpful discussions. This research was supported by the DAPRA Quest Program under grant No. N66001-09-1-2027.

[1] W. G. van der Wiel, S. De Franceschi, J. M. Elzerman, T. Fujisawa, S. Tarucha, and L. P. Kouwenhoven. *Rev. Mod. Phys.* **75**, 1 (2003).
[2] R. Hanson, L. P. Kouwenhoven, J. R. Petta, S. Tarucha, L. M. K. Vandersypen. *Rev. Mod. Phys.* **79**, 1217 (2007).
[3] F. A. Zwaneburg, A. S. Dzurak, A. Morello, M. Simmons, L. C. L. Hollenburg, G. Klimeck, S. Rogge, S. N. Coppersmith, and M. A. Eriksson. *Rev. Mod Phys.* **85**, 961, 2013
[4] T. Hayashi, T. Fujisawa, H. D. Cheong, Y. H. Jeong, and Y. Hirayama. *Phys. Rev. Lett.* **91**, 226804 (2003).
[5] Z. Shi, C. B. Simmons, D. R. Ward, J. R. Prance, R. T. Mohr, T. S. Koh, J. K. Gamble, X. Wu, D. E. Savage, M. G. Lagally, M. Friesen, S. N. Coppersmith, and M. A. Eriksson. *Phys. Rev. B* **88**, 075416 (2013)
[6] K. Wang, C. Payette, Y. Dovzhenko, P. W. Deelman, and J. R. Petta. *Phys. Rev. Lett.* **111**, 046801 (2013)
[7] J. R. Petta, A. C. Johnson, J. M. Taylor, E. A. Laird, A. Yacoby, M. D. Lukin, C. M. Marcus, M. P. Hanson, and A. C. Gossard. *Science* **309**, 2180 (2005).
[8] B. M. Maune, M. G. Borselli, B. Huang, T. D. Ladd, P. W. Deelman, K. S. Holabird, A. A. Kiselev, I. Alvarado-Rodriguez, R. S. Ross, A. E. Schmitz, M. Sokolich, C. A. Watson, M. F. Gyure, and A. T. Hunter. *Nature* **481**, 344 (2012).
[9] D. J. Reilly, C. M. Marcus, M. P. Hanson, and A. C. Gossard. *Appl. Phys. Lett.* **91**, 162101 (2007)
[10] A. Wallraff, D. I. Schuster, A. Blais, L. Frunzio, R. -S. Huang, J. Majer, S. Kumar, S. M. Girvin, and R. J. Schoelkopf. *Nature* **431** 162 (2004)
[11] A. Blais, R. -S. Huang, A. Wallraff, S. M. Girvin, and R. J. Schoelkopf. *Phys. Rev. A*, **69**, 062320 (2004)
[12] A. A. Clerk, M. H. Devoret, S. M. Girvin, Florian Marquardt, and R. J. Schoelkopf. *Rev. Mod. Phys.* **82** 1155 (2010).
[13] L. DiCarlo, M. D. Reed, L. Sun, B. R. Johnson, J. M. Chow, J. M. Gambetta, L. Frunzio, S. M. Girvin, M. H. Devoret, and R. J. Schoelkopf. *Nature*, **467**, 574 (2010).
[14] M. Hatridge, S. Shankar, M. Mirrahimi, F. Schackert, K. Geerlings, T. Brecht, K. M. Sliwa, B. Abdo, L. Frunzio, S. M. Girvin, R. J. Schoelkopf, and M. H. Devoret, *Science* **339**, 6116 (2013).
[15] A. A. Houck, D. I. Schuster, J. M. Gambetta, J. A. Schreier, B. R. Johnson, J. M. Chow, L. Frunzio, J. Majer, M. H. Devoret, S. M. Girvin, and R. J. Schoelkopf. *Nature*, **449**, 328 (2007).
[16] K. W. Murch, U. Vool, D. Zhou, S. J. Weber, S. M. Girvin, and I. Siddiqi. *Phys. Rev. Lett.* **109**, 3078 (2012).
[17] R. Vijay, C. Macklin, D. H. Slichter, S. J. Weber, K. W. Murch, R. Naik, A. N. Korotkov, and I. Siddiqi. *Nature* **490**, 77 (2012).
[18] T. Frey, P. J. Leek, M. Beck, A. Blais, T. Ihn, K. Ensslin, and A. Wallraff. *Phys. Rev. Lett* **108**, 046807 (2012).
[19] H. Toida, T. Nakajima, and S. Komiyama. *Phys. Rev. Lett.* **110**, 066802 (2013).
[20] P. Y. Yu, and M. Cardona. *Fundamentals of Semiconductors*, 3rd ed., Springer-Verlag, Berlin (2001)
[21] A. M. Tryryshkin, S. Tojo, J. J. L. Morton, H. Riemann, N. V. Abrosimov, P. Becker, H. -J. Pohl, T. Schenkel, M. L. W. Thewalt, Kohei M. Itoh, and S. A. Lyon. and I. Siddiqi, *Nature Mater.* **11**, 143 (2012).
[22] M. Xiao, M. G. House, and H. -W. Jiang. *Phys. Rev. Lett.* **104**, 096801 (2010).
[23] A. Morello, J. J. Pla, F. A. Zwanenburg, K. W. Chan, K. Y. Tan, H. Huebl, M. Möttönen, C. D. Nugroho, C. Yang, J. A. van Donkelaar, A. D. C. Alves, D. N. Jamieson, C. C. Escott, L. C. L. Hollenberg, R. G. Clark, and A. S. Dzurak. *Nature* **467**, 687 (2010)
[24] G. Salis, G. Salis, Y. Kato, K. Ensslin, D. C. Driscoll, A. C. Gossard and D. D. Awschalom. *Nature* **414**, 619 (2001)
[25] K. C. Nowack, F. H. L. Koppens, Yu. V. Nazarov, and L. M. K. Vandersypen. *Science* **318**, 1430 (2007)
[26] M. Pioro-Ladrière, T. Obata, Y. Tokura, Y.-S. Shin, T. Kubo, K. Yoshida, T. Taniyama, and S. Tarucha. *Nature Phys.* **4**, 776 (2008).
[27] K. D. Petersson, L. W. McFaul, M. D. Schroer, M. Jung, J. M. Taylor, A. A. Houck, and J. R. Petta. *Nature* **490**, 330 (2012)
[28] L. A. Tracy, E. P. Nordberg, R. W. Young, C. Borrs Pinilla, H. L. Stalford, G. A. Ten Eyck, K. Eng, K. D. Childs, J. R. Wendt, R. K. Grubbs, J. Stevens, M. P. Lilly, M. A. Eriksson, and M. S. Carroll. *Appl. Phys. Lett.* **97**, 192110 (2010)
[29] M. G. House, H. Pan, M. Xiao, and H. W. Jiang. *Appl. Phys. Lett.* **99**, 112116 (2011)
[30] N. S. Lai, W. H. Lim, C. H. Yang, F. A. Zwanenburg, W. A. Coish, F. Qassemi, A. Morello and A. S. Dzurak. *Sci. Rep.* **1**, 1 (2011).
[31] C. C. Lo, C. D. Weis, J. van Tol, J. Bokor, and T.

Schenkel. *Phys. Rev. Lett.* **110**, 057601 (2013).
[32] T. Ando, A. B. Fowler and F. Stern. *Rev. Mod. Phys.* **54**, 437 (1982)
[33] Thomas Ihn. *Semiconductor Nanostructures*, Oxford University Press, Oxford (2010)
[34] S. M. Sze and K. K. Ng *Physics of Semiconductor Devices*, 3rd Ed.,Wiley-Interscience, Hoboken, NJ (2007)
[35] COMSOL, Inc. http://www.comsol.com
[36] L. Childress, A. S. Srensen and M. D. Lukin. *Phys. Rev. A* **69**, 042302 (2004)
[37] D. H. Slichter, O. Naaman, and I. Siddiqi. *Appl. Phys. Lett.* **94**, 192508 (2009)
[38] J. M. Martinis, K. B. Cooper, R. McDermott, M. Steffen, M. Ansmann, K. D. Osborn, K. Cicak, Seongshik Oh, D. P. Pappas, R. W. Simmonds, and C. C. Yu. *Phys. Rev. Lett.* **95**, 210503 (2005)
[39] A. D. OConnell, M. Ansmann, R. C. Bialczak, M. Hofheinz, N. Katz, E. Lucero, C. McKenney, M. Neeley, H. Wang, E. M. Weig, A. N. Cleland, and J. M. Martinis. *Appl. Phys. Lett.* **92**, 112903 (2008)